

A Radio-Frequency Emitter Design for the Low-Frequency Regime in Atomic Experiments

Yudong Wei,^{1,2, a)} Zhongshu Hu,^{1,2} Yajing Guo,^{1,2} Zhentian Qian,^{1,2} Shengjie Jin,^{1,2, b)} Xuzong Chen,³ and Xiong-jun Liu^{1,2,4}

¹⁾International Center for Quantum Materials, School of Physics, Peking University, Beijing 100871, China

²⁾Hefei National Laboratory, Hefei 230088, China

³⁾School of Electronics Engineering and Computer Science, Peking University, Beijing 100871, China

⁴⁾International Quantum Academy, Shenzhen 518048, China

Radio frequency (RF) control is a key technique in cold atom experiments. Here, we present a new design based on virtual load, where a low-frequency coil with a frequency of up to 30 MHz, functions as both an inductor and a power-sharing element in a capacitive transformer circuit. This design enables a highly efficient RF circuit with tunable matching bandwidth. It integrates broadband and narrowband coils into a compact configuration, overcoming the distance limitations of metallic chambers. The broadband RF system, tested in a 10-second evaporative cooling experiment, reduced input power from 14.7 dBW to -3.5 dBW due to its low-pass behavior, effectively cooling the Bose-Fermi mixture to below 10 μ K. The narrowband RF system was tested in a Landau-Zener experiment and transferred 80% of Rb atoms from $|F = 2, m_F = 2\rangle$ to $|2, -2\rangle$ in 1 second, yielding a Rabi frequency of 7.6 kHz at 0.1 dBW. The power-sharing properties of the virtual load ensure impedance closely matches the ideal lumped-element simulations, demonstrating the design's robustness to disturbances.

I. INTRODUCTION

In experiments focused on preparing ultracold alkali metal atoms and molecules, a common approach involves trapping atomic ensembles at micro-Kelvin temperatures in a magneto-optical trap (MOT) followed by confinement in an anti-Helmholtz magnetic trap. Simultaneously, RF field is employed to remove high-energy atoms from the tail of the Maxwell-Boltzmann distribution by transferring them to high-field-seeking states, thereby forcing their ejection¹⁻³. Typically, when the timescale of RF decrease is longer than the thermal equilibration time of the atomic ensemble, this process can lower the temperature of the atoms by an order of magnitude or more, providing a foundation for further evaporative cooling in optical traps. If the phase-space density is high enough, the atomic ensemble can be evaporatively cooled directly into a quantum degeneracy⁴⁻⁶.

For alkali metals, there are typically two options used in magnetic trap evaporation: the first involves RF transitions between sublevels within the same hyperfine structure, while the second involves transferring atoms to another hyperfine level of the ground state using microwaves. The former option usually requires frequencies below 30 megahertz (MHz), which are easier to generate. However, low-frequency coils tend to have a high quality factor (Q), making impedance matching a significant challenge. As a result, the transmission efficiency becomes uneven across the frequency range for evaporative cooling. This not only extends the evaporation time to tens of seconds⁷⁻¹¹, causing unnecessary atom loss, but also increases the likelihood of electromagnetic interference. The latter option, with resonant frequencies reaching the microwave range, requires specialized sources and equipment. Additionally, antennas¹² impose stricter impedance matching

requirements, including the wiring of connection cables and circuit layout^{13,14}. Furthermore, an additional microwave at different frequency is needed to remove certain intermediate atomic states during evaporative cooling, in order to reduce the probability of harmful inelastic collisions^{15,16}.

In this paper, we present a simple yet effective design for the matching circuit of a low-frequency coil inspired by Ref. 17, where a virtual load is used as the matching terminal to allow the coil to achieve higher current. Nonetheless, this approach is not suitable for the ultra-low-frequency range. In our version, the coil is treated as an inductive element, forming part of a capacitive transformer. The terminal is balanced with a virtual load that dissipates excess power, enabling the design to achieve a flexible and stable matching bandwidth. The transmission power achieved with this design is 2 to 3 times higher than that of a conventional setup in evaporative cooling, where the coil is directly connected in series with a resistive load¹⁸.

This design offers several advantages: first, the coil is connected to the circuit in the simplest way, with only two soldering points, significantly reducing transmission losses. Second, using a virtual load to match the power amplifier simplifies the matching process, promoting a stable and low reflection coefficient while streamlining impedance adjustments during experiments. Additionally, as the matching network operates as a low-pass resonant circuit, the RF coil works even at relatively low frequencies. These advantages make the design well-suited for evaporative experiments requiring broadband matching and internal state manipulations that demand high peak currents.

The design enabled us to reduce the temperature of Rubidium-87 and Potassium-40 (⁸⁷Rb-⁴⁰K) mixtures trapped in a magnetic trap, from 260(12) μ K to 9(2) μ K within 10 seconds, while preserving the number of ⁴⁰K atoms with minimal loss. Subsequently, after transferring the mixtures into optical dipole trap, we achieved double degeneracy starting with a magneto-optical trap (MOT) containing merely 2 mil-

^{a)}weiyd2017@pku.edu.cn

^{b)}jinshengjie@pku.edu.cn

lion ^{40}K atoms. We also tested the narrowband version of the coil, achieving a Rabi frequency of approximately 7.6 kHz on the ground state of Rb atoms with an input power of only 0.1 dBW. Moreover, the effect of the coil material and shape on design performance is considered during our discussion.

II. DESIGN AND CONFIGURATION

The conventional L-network matching technique is widely used in RF circuits for impedance matching due to its simplicity, reliability, low loss, and cost-effectiveness¹⁹. However, when applied to an emitter operating at low frequency, several issues arise. Let the coil impedance and power source resistance be $R_C + iX_C$ and R_S , respectively. In atomic experiments, the coil's reactance is generally much greater than its resistance, resulting in a quality factor for the entire resonant circuit given by $Q \propto X_C/\sqrt{R_S R_C}$ ^{19,20}. Here, the reactance in the experiment is mainly contributed by the inductance, causing the circuit's Q value to decrease as frequency lowers. Unfortunately, even at its lowest, the Q factor remains on the order of $\sqrt{R_S/R_C} - 1$, which is still much greater than unity (see Fig. 1 for details). A high Q value restricts the bandwidth of the resonant circuit, leading to substantial impedance mismatches over a wide frequency range, which substantially raises the risk of damaging the driving system.

Other issues at low frequencies include the significant disparity between the internal resistance and the coil's resistance, making it challenging to achieve the necessary impedance transformation, which often requires a factor of tens. Meanwhile, low-pass matching circuits rely on inductive elements, whose resistance is often comparable to that of the coil, resulting in unavoidable energy losses and electromagnetic radiation.

The above issues also arise in conventional transformer circuits, such as mutual inductance-based designs. The capacitive transformer circuit naturally facilitates ultra-low-frequency coil design, providing not only wide-range impedance transformation but also minimizing the use of inductive elements. In our approach, the coil itself serve as the inductor of the matching circuit, with a virtual load at the terminal to match the internal resistance. The voltage division effect of the virtual load will significantly simplify impedance matching optimization.

A. General properties

The impedance of an RF coil primarily consists of both resistance and inductive reactance, $\chi_C = R_C + i\omega L_C$. Here we need to optimize the current through the coil, so the resistance must be taken into account. The matching circuit is shown in the Fig. 1(a). The conjugate matching condition for resonance is given by²⁰:

$$\begin{aligned} R_{\text{in}} &= R_S, \\ \frac{1}{\omega_0 L_C} &= \frac{\omega_0 C_1 C_2}{C_1 + C_2}, \end{aligned} \quad (1)$$

and here we define $R_{\text{in}} \equiv \tilde{R}_C \parallel \tilde{R}_L$ as the effective resistance resulting from the coil and virtual load with R_S (typically 50 Ω) being internal resistance of amplifier. The

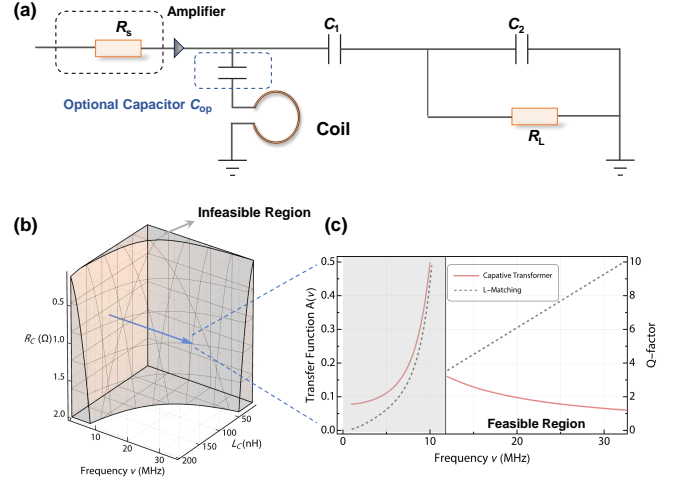


FIG. 1. Schematic of the capacitive transformer network for matching a low-frequency RF coil, with C_{op} as an optional capacitor, replaced by a wire in other cases. (a) The RF coil serves as the inductor, canceling the reactance introduced by the capacitors used for voltage division. (b) The shaded area shows the parameter range where perfect resonance cannot be achieved according to Eq. 1, thereby small L_C and large R_C prevent the achievement of optimal impedance matching. Note the shaded area is also determined by optional capacitor (see Section II B). (c) Comparison of the Q -factor as a function of frequency for the dual-capacitor L-network and the capacitive transformer network when resonance is achieved (above $\nu_{\text{crit}} = 11.5$ MHz). Below ν_{crit} , neither circuit achieves exact resonance. Using parameters at ν_{crit} , the transfer function below this frequency shows the low-pass behavior of our design. Parameters for (c) are $L_C = 100$ nH, $R_C = 1$ Ω , and $R_S = R_L = 50$ Ω .

terms \tilde{R}_C and \tilde{R}_L are given by $\tilde{R}_C \equiv [R_C^2 + (\omega L_C)^2]/R_C$ and $\tilde{R}_L \equiv (C_1 + C_2)^2/C_1^2 R_L$, respectively. When the resonance frequency ω_0 satisfies $\omega + \omega_0 \gg |\omega - \omega_0|$, the transfer function $A(\omega)$ of the whole capacitive transformer near the resonance frequency simplifies to :

$$A(\omega) \approx \frac{R_{\text{in}}}{R_{\text{in}} + R_S} \left[\frac{1}{1 + i2Q(\omega - \omega_0)} \right] \quad (2)$$

with Q -factor being $Q \equiv \frac{R_{\text{in}} \parallel R_S}{\omega_0 L_C}$. The internal resistance is generally fixed, making the frequency-dependent Q factor directly related to the inductance of the coil. Small coils commonly used in experiments have inductances on the order of hundreds of nH^{17,21–23}. In the low-frequency regime, such feature allows the Q factor to remain within one order of magnitude, providing both physical flexibility and ease of realization.

B. Current Characteristics

Our goal is to maximize power transfer from the source to the coil under impedance matching conditions. By selecting an appropriate capacitor, the effective resistance of the virtual load near resonance can be increased, ensuring $\tilde{R}_L \gg \tilde{R}_C$. This minimizes power dissipation, thus enhances the current through the coil. We first examine how to optimize the current in a capacitive transformer. Then in the following section, we

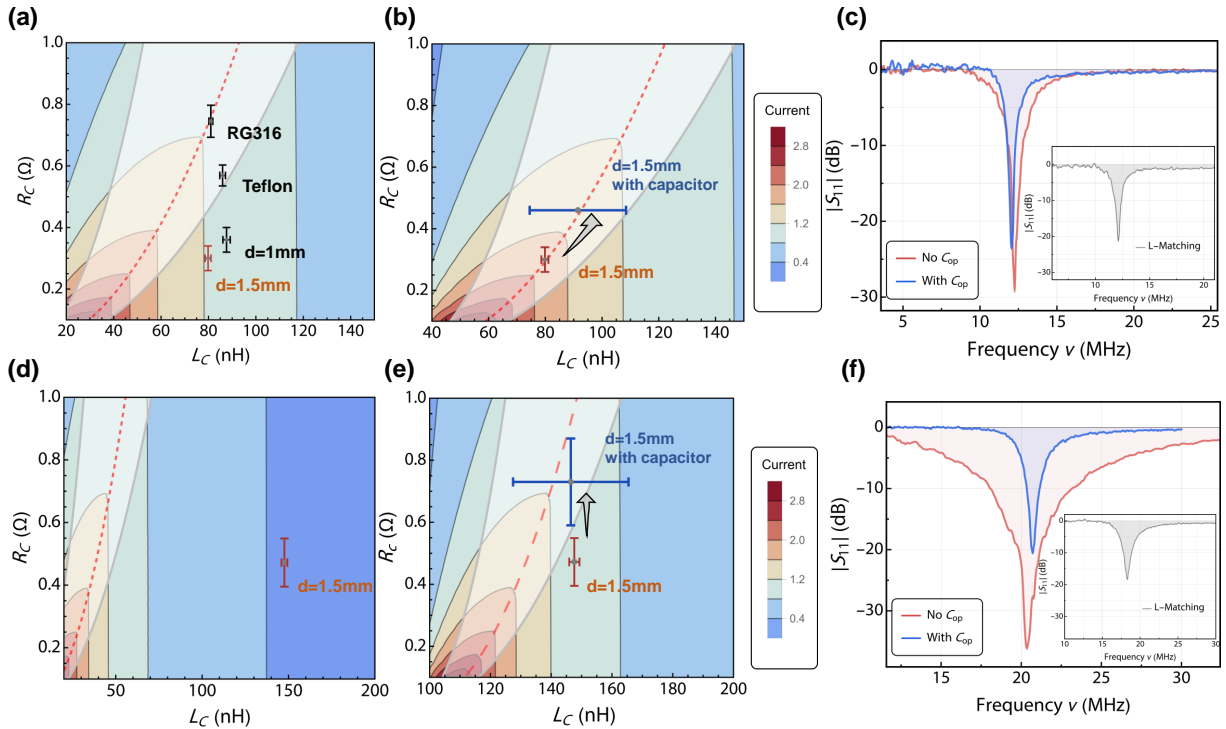


FIG. 2. Current distribution and impedance matching for different inductances L_C and resistances R_C of the RF coil under resonant conditions at 12 MHz (the first row) and 20 MHz (the second row). (a) Four coil materials with different resistances and inductances. The enameled copper wire ($d = 1.5$ mm) has the lowest resistance but lies to the right of the red dashed line. The region neither satisfies the resonance condition of Eq. (1) at 12 MHz or achieves good impedance matching (outside the white region, see text). (b) Adding an optional capacitor C_{op} shifts the current distribution, resonance solution region, and impedance matching region along the inductance axis. This adjustment allows the enameled copper wire to achieve resonance, optimal impedance matching, and higher current flow. (c) $|S_{11}|$ before and after adding C_{op} , with the inset showing results for a conventional L-network. (d), (e), and (f) repeat the resonance at about 20 MHz. Parameters are (a) $C_1 = 5.6$ nF, $C_2 = 3.3$ nF and (b) $C_1 = 3.3$ nF, $C_2 = 10$ nF, $C_{op} = 5.6$ nF. Parameters for (d) and (e) are $C_1 = 15$ nF, $C_2 = 0.36$ nF and $C_1 = 3.3$ nF, $C_2 = 1.8$ nF, $C_{op} = 0.56$ nF, respectively. All points are obtained by fitting the measured $|S_{11}|$ curves. Coils are circular with a diameter of 4.1 cm for (a)(b)(c) and 6 cm for the others. Both consist of a single turn.

discuss how to achieve a smoothly varying RF strength over a wide frequency range for evaporative cooling experiments.

In Fig. 2, we plot the current through the coil for different values of R_C and L_C at fixed frequencies of 12 MHz and 20 MHz under resonant conditions. The red dashed line represents the condition where $\tilde{R}_C = 1/R_s \ll \tilde{R}_L$, indicates that nearly all of the power is delivered to the coil, corresponding to the maximum achievable current. Moreover, the resonance equation in Eq. (1) allows solutions to the left of the red dashed line. To the right of the red dashed line, since $\tilde{R}_C, \tilde{R}_L > 1/R_s$, no physical solutions satisfy exact resonance. Therefore we use the parameters²⁴ on the red dashed line for the plot. The white area highlights the most efficient parameter range for the RF coil, where it captures over 75% of the maximum output power from the amplifier.

For a narrowband emitter, it is key to ensure that the parameters fall within the white region. Without using an optional capacitor, the parameters can be modified by different materials, i.e. effectively shifts the R_C and L_C . In Fig. 2(a), we consider common materials used in atomic experiments, including enameled copper wire with diameters of 1 mm and 1.5 mm, Teflon-coated tinned wire, and the braided layer of RG316 cables. While the inductance of these materials varies slightly for the same shape, their resistances differ obviously.

The thicker enameled copper wire exhibits the smallest resistance, but at low frequencies, it often fails to achieve optimal impedance matching (it falls to the right of the red dashed line in Fig. 2(a)). RG316, on the other hand, has a higher resistance and lies exactly on the red dashed line, allowing for optimal impedance matching. However, its higher resistance prevents an increase in current flow.

To further increase the current, we place an optional capacitor in series with the 1.5 mm enameled copper wire. This capacitor effectively shifts the current distribution pattern in Fig. 2(a) along the inductive axis, as shown in Fig. 2(b). In this case, the R_C and L_C of the enameled copper wire coil (marked in blue) slightly increase due to the soldering resistance but remain near the shifted red dashed line, achieving the ideal maximum current. Fig. 2(c) shows the magnitude of S_{11} curves before and after the adding the optional capacitor. The width of dip for the latter narrows, while the resonance frequency remains nearly unchanged, demonstrating the validity of Eq. (1). Similarly, we tested a resonance frequency at 20 MHz, confirming that adding the optional capacitor effectively maintained the current through the coil while improving impedance matching.

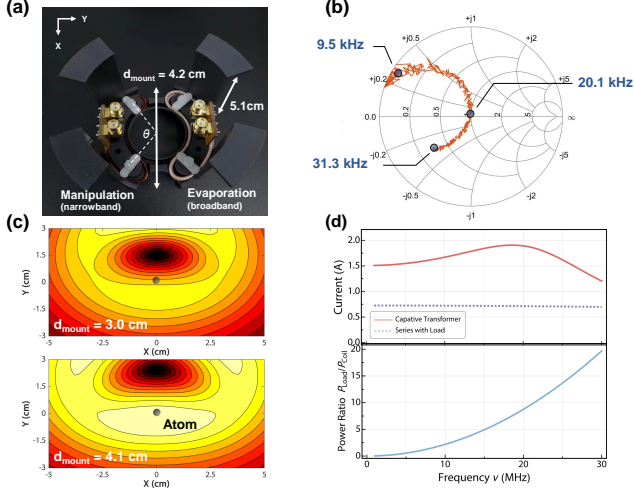


FIG. 3. Configuration of the two coils (RG316 and copper wire) for evaporative cooling and sublevel manipulation, with impedance matching measurements and simulations for the former(right) coil. (a) The two half-annular coils are mounted on a resin holder, positioned close to the atoms and avoiding contact with the upper viewport. (b) Measured Smith chart with key frequencies labeled. The measurement errors increase below 8 kHz. The magnitude of S_{11} is similar to the red curve in Fig. 2(g). (c) Simulated horizontal electromagnetic field at atoms, showing how adjusting the coil's outer diameter modifies the field distribution. Brighter colors represent higher intensity. (d) Simulated current and power through the evaporation coil as a function of frequency, with an input power of 1 W. The smoother current variation is attributed to the power redistribution between the virtual load and the coil. Impedance mismatch at ultra-low frequencies is not a concern as the input RF power at these frequencies has already decreased by two orders of magnitude (see Fig. 4(b)). The electronic components used are $R_C \approx 0.7 \Omega$, $L_C \approx 175 \text{ nH}$, and dual capacitors $C_1 = 4.7 \text{ nF}$, $C_2 = 0.3 \text{ nF}$ for evaporation, and $R_C \approx 0.35 \Omega$, $L_C \approx 275 \text{ nH}$, $C_1 = 10 \text{ nF}$, $C_2 = 15 \text{ nF}$ for sublevel manipulation, respectively.

III. THE COILS IN EXPERIMENTS

We then validate the performance of the circuit design in cold atom experiments, including evaporative cooling and Landau-Zener tunneling within a Rb-K hybrid atomic system confined in a magnetic trap. To meet the requirements for evaporation, we carefully selected the coil length and material. This choice, at the cost of sacrificing peak current, provided a broad bandwidth for impedance matching, ensuring smooth current variation across the entire RF range. Nevertheless, for manipulating sublevels within the same hyperfine state under weak magnetic fields, it is crucial for the coil to allocate as much power as possible in the low-frequency region to maximize the peak current.

A. The Evaporation

The simplest choice for the coil shape is either circular or half-annular^{17,25}. Considering the extremely limited space around the upper and lower viewports in metal chambers, we chose the half-annular design which leaves room for an additional RF coil for rapid sublevel control, as shown in Fig. 3(a). Referring to Fig. 2(e), when the inductance is large, the mag-

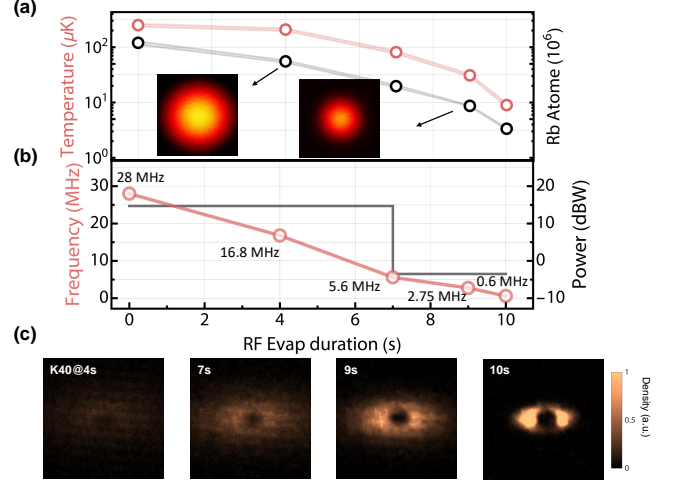


FIG. 4. RF evaporative cooling of a Bose-Fermi mixture in a magnetic trap. (a) The variation in ^{87}Rb atom number and temperature over four stages. Atom number decreases from 1.2×10^7 to 3.8×10^5 , while the temperature drops from $260(12) \mu\text{K}$ to $9(2) \mu\text{K}$, with bands denoting the standard deviation. (b) RF frequency decreases nearly linearly from 28 MHz to 0.6 MHz over 10 seconds. The power is reduced by a factor of 10^2 (from 14.7 dBW to -3.5 dBW) in the last two stages to minimize atom loss, despite the coil maintaining substantial current at ultra-low frequencies. (c) In-situ imaging of ^{40}K atoms at each stage reveals a significant increase in density. The plug beam has a waist of $40 \mu\text{m}$, a power of 800 mW, and a wavelength of 760 nm. The magnetic trap gradient is maintained at 150 G/cm throughout the evaporation.

nitude of S_{11} spans a relatively wide range. We selected the braided layer of RG316 to reduce the current decay rate at lower frequencies, and the measured S_{11} curves and current simulation results are shown in Fig. 3(b)(d). As the RF decreases, the current changes smoothly, and compared to the configuration where the coil is connected in series with a load of similar internal resistance, the current increases by two to three times. Considering the space limitations, we fixed the inner radius of the coil and set the opening angle at $\theta \approx 110^\circ$. Therefore, to optimize the maximum RF field at the atoms (located at a distance of 4.1 cm), we fine-tuned the outer diameter of the half-annular coil. This modification significantly altered the electromagnetic field distribution at the atomic position, as shown in Fig. 3(c).

In the experiment, we loaded about 1.2×10^7 ^{87}Rb atoms in the $|F=2, m_F=2\rangle$ and about 2×10^5 ^{40}K atoms in the $|9/2, 9/2\rangle$ into a 150 G/cm optical-plugged magnetic trap. The initial temperature of the ^{87}Rb atoms was around $260 \mu\text{K}$. Keeping the trap depth constant, we performed RF evaporation in four stages by gradually lowering the RF and power. After these stages, the temperature of the ^{87}Rb atoms markedly decreased to below $10 \mu\text{K}$. Meanwhile, the density of the ^{40}K atoms increased, with no noticeable loss in total atom count, ultimately reaching the same temperature as the Rb atoms.

Fig. 4(a) shows the variation in atom numbers for both species as a function of RF and power. The insets show the momentum distribution of Rb atoms after the first and third evaporation stages, indicating thermal equilibrium was reached, which suggests the potential for further reducing

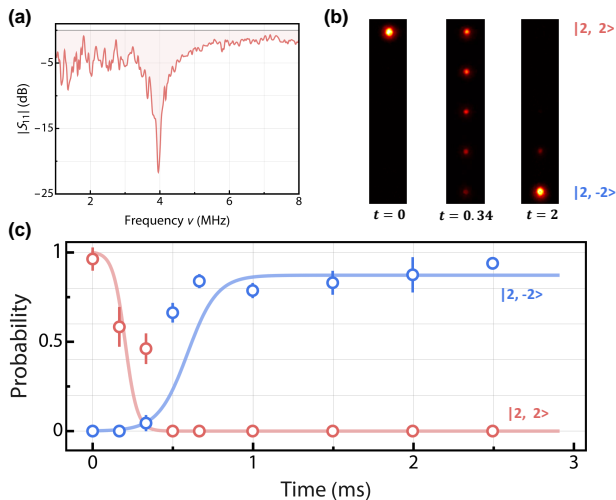


FIG. 5. Measurement of reflection coefficient for narrowband coil and Landau-Zener tunneling for $F = 2$ Zeeman sublevels of Rb BEC. (a) The minimum value of $|S_{11}|$ appears about 4 MHz, and the low-pass characteristic is again maintained. (b)(c) Measuring the population transfer of Rb atoms from $|2, 2\rangle$ (red circles) to $|2, -2\rangle$ (blue circles) by Stern-Gerlach method. The error bars represent the standard deviation of the data. The solid lines represent the numerical simulation governed by Sigmoid function, where rapid dynamics are smoothed for clarity. The data are normalized to the initial atom number, with the magnetic field being linearly reduced over 2.9 ms (see text) while keeping the RF fixed at 3.91 MHz of 0.1 dBW. The value of magnetic field gradient precisely balances the gravitational force on the $|2, 2\rangle$ atoms.

evaporation time (see Appendix A). Meanwhile, the density of ^{40}K atoms gradually increased at each stage, as shown in Fig. 4(c). Due to the fewer potassium atoms and their segmented distribution caused by the plug beam, we could not accurately measure their temperature in the trap. However, in the subsequent optical trap, we confirmed that the temperatures of the two species were consistent²⁶. The gradual variation of current in the coil facilitates the RF evaporation process, particularly simplifying the tuning of RF intensity and sweep rate.

B. The Landau-Zener Manipulation

The section focuses on the coil's performance in a narrowband regime, where optimizing the peak current is the primary objective. At the same time, it is essential to maintain a high level of impedance matching to ensure the design remains suitable for high-power application. To reduce the coil's resistance, we used enameled copper wire with $d=1.0$ mm diameter. At low frequencies, this design easily achieves both impedance matching and a high peak current without the need for an optional capacitor (see Fig. 2(a)(e)). In Fig. 5(a), we show the reflection coefficient at the input port of the circuit, which reaches approximately -22 dB near 4 MHz.

Near the optimal emission frequency of the coil, only a weak magnetic field is needed to bring the hyperfine sublevels into resonance. However, due to the minimal corrections from the quadratic Zeeman effect, it is difficult to directly mea-

sure the complete Rabi coupling between two isolated sublevels. Thus, we experimentally estimate the Rabi frequency using Landau-Zener tunneling. We first prepare a Rb Bose-Einstein condensate (BEC) in the $|2, 2\rangle$, with a condensate fraction slightly below 50%. The RF field is then abruptly turned on and maintained at a fixed frequency of 0.1 dBW, while the external field is linearly ramped down within 2.9 ms. This process effectively shifts the RF detuning from the $|2, 2\rangle$ to $|2, 1\rangle$ transition, starting with an initial red detuning of approximately 15 kHz and ending with a final blue detuning of around 105 kHz. The evolution of the initial state $|2, 2\rangle$ and the final state $|2, -2\rangle$ during this process is shown in Fig. 5(b)(c), with the transfer rate exceeding 90%.

Compared to the simulation of the averaged dynamics of Landau-Zener tunneling (solid lines in Fig. 5(c)), we find that the Rabi frequency is around 7.6 kHz. Additionally, approximately 80% of the atoms are transferred to the $|2, -2\rangle$ state within 1 ms, with no significant decrease in optical density. Moreover, we emphasize that the narrowband design can cover frequencies below 30 MHz, making it suitable for various RF techniques for controlling Zeeman sublevels.

IV. CONCLUSIONS

In this paper, we presented a matching circuit design for low-frequency (below 30 MHz) and high-power RF systems, suitable for a variety of cold atom experiments. By treating the coil as an inductor rather than a terminal load, we developed both broadband and narrowband matching circuits. The broadband circuit, validated in a Bose-Fermi dual-component evaporation experiment, provides a smoothly varying current, greatly simplifying the adjustment of evaporation timing. The narrowband one, tested in Landau-Zener experiment, demonstrated its potential for achieving high Rabi frequencies and rapid control, with applications in Rabi pulse-based spectroscopy²⁷⁻²⁹ and interferometry³⁰⁻³².

To overcome the spatial distance limitations posed by metallic chamber, we designed a double-coil mount that maximizes space utilization near the viewport while reducing RF electromagnetic interference. This design offers robust and precise frequency matching, ensuring that the emission frequency remains stable, unaffected by environmental factors or wiring complexities. Beyond typical alkali-metal experiments, its features make it especially well-suited for more complex experimental environments, such as cold atom experiments on the space station.

ACKNOWLEDGMENTS

We thank Xinyi Huang and Mingcheng Liang for insightful comments and discussions. We also thank Pengju Zhao for assistance with the cold atom experiments. This work was supported by National Key Research and Development Program of China (2021YFA1400900), the National Natural Science Foundation of China (Grants No. 12425401 and No. 12261160368), the Innovation Program for Quantum Science and Technology (Grant No. 2021ZD0302000), and the Shanghai Municipal Science and Technology Major Project (Grant No. 2019SHZDZX01).

Appendix A: Estimate the efficiency for evaporation

We also explored the possibility of further reducing the evaporation time. The evaporation efficiency factor is defined as $\gamma \equiv \ln(T/T_0)/\ln(N/N_0)$, where T_0, N_0 are the initial temperature and atom number, respectively and T, N are their values during evaporation. We found $\gamma \approx 1$ for the entire Bose-Fermi mixture for the whole RF evaporation, with the lowest values of around 0.7 in the first two stages. At the end of the first stage, the ratio of elastic to inelastic collision rate in the magnetic trap is approximately $R = K_e/K_{\text{ine}} \approx 674$. To maintain effective cooling, the minimum ratio required is $R_{\text{min}} \approx 530$, then we obtain $R/R_{\text{min}} \approx 1.3^{33,34,35}$. The efficiency at this stage is just slightly above the threshold, which may be due to the fact that the strength of our magnetic gradient is limited to around 50%–70% of that applied by other groups^{11,36–38}. A deeper trap would compress the atomic cloud, thereby increasing the elastic collision rate $K_e \propto r_0^{-3}$ with r_0 being the radius of the mixture. Moreover, in the trap center, where R/R_{min} exceeds 10, the evaporation efficiency could be further enhanced at this stage.

- ¹W. Ketterle and N. V. Druten (Academic Press, 1996) pp. 181–236.
- ²G. Modugno, G. Ferrari, G. Roati, R. J. Brecha, A. Simoni, and M. Inguscio, *Science* **294**, 1320 (2001).
- ³P. Bouyer, V. Boyer, S. Murdoch, G. Delannoy, Y. Le Coq, A. Aspect, and M. Lécroivain, “Rf-induced evaporative cooling and BEC in a high magnetic field,” in *Bose-Einstein Condensates and Atom Lasers*, edited by S. Martellucci, A. N. Chester, A. Aspect, and M. Inguscio (Springer US, Boston, MA, 2002) pp. 165–186.
- ⁴M. H. Anderson, J. R. Ensher, M. R. Matthews, C. E. Wieman, and E. A. Cornell, *Science* **269**, 198 (1995).
- ⁵K. B. Davis, M. O. Mewes, M. R. Andrews, N. J. Van Druten, D. S. Durfee, D. M. Kurn, and W. Ketterle, *Physical Review Letters* **75**, 3969 (1995).
- ⁶B. DeMarco and D. S. Jin, *Science* **285**, 1703 (1999).
- ⁷P. Ding, B. Shan, Y. Zhao, Y. Yang, L. Chen, Z. Meng, P. Wang, and L. Huang, *Chinese Physics B* **33**, 063402 (2024).
- ⁸M. E. Gehm, *Preparation of an Optically-Trapped Degenerate Fermi Gas of ^6Li : Finding the Route to Degeneracy*, Ph.D. thesis, Duke University (2003).
- ⁹G. Roati, F. Riboli, G. Modugno, and M. Inguscio, *Physical Review Letters* **89**, 150403 (2002).
- ¹⁰P.-J. Wang, D.-Z. Xiong, Z.-K. Fu, and J. Zhang, *Chinese Physics B* **20**, 016701 (2011).
- ¹¹T. Stöferle, *Exploring Atomic Quantum Gases in Optical Lattices*, Ph.D. thesis, Swiss Federal Institute of Technology (2005).
- ¹²We refer to devices that emit microwave (about gigahertz) as antennas.
- ¹³O. Elalaoui, M. E. Ghzaoui, and J. Foshi, *Materials Science and Engineering: B* **304**, 117382 (2024).
- ¹⁴Firdaus, L. Monica, and Yustini, *IOP Conference Series: Materials Science and Engineering* **846**, 012013 (2020).
- ¹⁵G. Modugno, M. Modugno, F. Riboli, G. Roati, and M. Inguscio, *Physical Review Letters* **89**, 190404 (2002).
- ¹⁶L. De Marco, G. Valtolina, K. Matsuda, W. G. Tobias, J. P. Covey, and J. Ye, *Science* **363**, 853 (2019).
- ¹⁷F. Scazza, G. Del Pace, L. Pieri, R. Concas, W. J. Kwon, and G. Roati, (2021), arXiv:2104.12730.
- ¹⁸Y. Cohen, *Radio-Frequency Atomic Magnetometry with a Rubidium Bose-Einstein Condensate*, Ph.D. thesis, University College London (2021).
- ¹⁹C. A. Balanis, *Antenna Theory Analysis and Design* (Wiley, 2016).
- ²⁰C. Coleman, *An Introduction to Radio Frequency Engineering* (Cambridge, 2005).
- ²¹D. S. Barker, A. Restelli, J. A. Fedchak, J. Scherschligt, and S. Eckel, *Review of Scientific Instruments* **91**, 104708 (2020).
- ²²K. Herb, J. Zopes, K. S. Cujia, and C. L. Degen, *Review of Scientific Instruments* **91**, 113106 (2020).
- ²³J. Mispelner, M. Lupu, and A. Briguet, *NMR Probeheads for Biophysical and Biomedical Experiments*, 2nd ed. (Imperial College Press, 2015).
- ²⁴Here, we still refer to the coil’s resistance R_C and inductance L_C as parameters, rather than the capacitors C_1 and C_2 .
- ²⁵D. Ciampini, E. Courtade, C. Sias, D. Cossart, G. Carelli, F. Mango, O. Morsch, and E. Arimondo, *Optics Communications* **257**, 340 (2006).
- ²⁶The transfer efficiency of fermionic potassium from the magnetic trap to the optical trap was about 50%, with losses primarily caused by segmentation effects from the plug beam.
- ²⁷L. Huang, Z. Meng, P. Wang, P. Peng, S.-L. Zhang, L. Chen, D. Li, Q. Zhou, and J. Zhang, *Nature Physics* **12**, 540 (2016).
- ²⁸X.-T. Xu, C.-R. Yi, B.-Z. Wang, W. Sun, Y. Deng, X.-J. Liu, S. Chen, and J.-W. Pan, *Science Bulletin* **63**, 1464 (2018).
- ²⁹X.-T. Xu, Z.-Y. Wang, R.-H. Jiao, C.-R. Yi, W. Sun, and S. Chen, *Review of Scientific Instruments* **90**, 054708 (2019).
- ³⁰M. Sadgrove, Y. Eto, S. Sekine, H. Suzuki, and T. Hirano, *Journal of the Physical Society of Japan* **82**, 094002 (2013).
- ³¹X. Ren, W. Yan, Y. Yang, X. Deng, W. Xu, Z. Hu, and M. Zhou, *Phys. Rev. A* **108**, 063309 (2023).
- ³²S. Tiengo, R. Eid, M. Apfel, G. Brulin, and T. Bourdel, (2025), arXiv:2501.11375.
- ³³P. Valkering, *Optimization of Evaporative Cooling of Rubidium Atoms in a Magnetic Trap*, Ph.D. thesis, University of Utrecht (1999).
- ³⁴D. J. Han, *Journal of the Physical Society of Japan* **76**, 023301 (2007).
- ³⁵The average elastic collision rate for the entire Rb atom cloud is given by $K_e = \sqrt{2}n\sigma v/8$, where n, σ and v represent the average density, s-wave scattering cross-section, and average velocity, respectively. The inelastic collision rate K_{ine} is primarily determined by background gas, and here we estimate it based on the collision rate of helium and atoms in a vacuum of 5×10^{-11} Torr. The minimum R required for sustained evaporative cooling is $R_{\text{min}} \equiv \lambda/[\gamma(\chi - 1/2) - 1]$, where λ, χ and η represent the ratio of evaporation time to elastic collision time, a trap shape-dependent parameter, and the trap truncation parameter, respectively.
- ³⁶J. Goldwin, S. Inouye, M. L. Olsen, B. Newman, B. D. DePaola, and D. S. Jin, *Physical Review A* **70**, 021601 (2004).
- ³⁷R. S. Bloom, *Few-Body Collisions in a Quantum Gas Mixture of 40K and 87Rb Atoms*, Ph.D. thesis, University of Colorado (2014).
- ³⁸M. Hachmann, *Degenerate Fermi gases in higher Bloch bands of a bipartite optical square lattice*, Ph.D. thesis, Universität Hamburg (2022).